

Article

Optimization of Nanofluid Flow and Temperature Uniformity in the Spectral Beam Splitting Module of PV/T System

Liwei Lu ¹, Rui Tian ^{1,2,*} and Xiaofei Han ¹

¹ College of Energy and Power Engineering, Inner Mongolia University of Technology, Hohhot 010051, China; 20171000025@imut.edu.cn (L.L.); shawnhan@nuaa.edu.cn (X.H.)

² Inner Mongolia Key Laboratory of Renewable Energy, Hohhot 010051, China

* Correspondence: tianr@imut.edu.cn

Abstract: The mass fraction of 0.01 wt% ZnO nanofluid was prepared via the two-step method. The measurement verifies that ZnO nanofluids have better transmission characteristics in the frequency division window range of 400–1200 nm. At the same time, it has good absorption characteristics in ultraviolet and near-infrared bands, which meets the application conditions of the spectral beam-splitting module of the PV/T system. A spectral beam-splitting module of the PV/T system was designed. The simplified physical model was established in ANSYS 14.0. The flow field and convective heat transfer were simulated for different arrangements of the interlayer inlet to obtain a more ideal and uniform temperature distribution to improve the system's comprehensive efficiency. The results show that the fluid flow in the interlayer under case II is more uniform, and the temperature field distribution is better than other arrangements. Hence, this work could provide a reference for optimising nanofluid flow within a spectral beam-splitting module.

Keywords: spectral beam splitting; nanofluid; PV/T; velocity distribution; temperature field



Citation: Lu, L.; Tian, R.; Han, X. Optimization of Nanofluid Flow and Temperature Uniformity in the Spectral Beam Splitting Module of PV/T System. *Energies* **2023**, *16*, 4666. <https://doi.org/10.3390/en16124666>

Academic Editor: Artur Bartosik

Received: 18 April 2023

Revised: 10 June 2023

Accepted: 11 June 2023

Published: 12 June 2023



Copyright: © 2023 by the authors. Licensee MDPI, Basel, Switzerland. This article is an open access article distributed under the terms and conditions of the Creative Commons Attribution (CC BY) license (<https://creativecommons.org/licenses/by/4.0/>).

1. Introduction

The rapid development of human society, the sharp decline of traditional fossil energy reserves and the adverse impact on the environment in the application process have posed new challenges to the sustainable development of human beings. The development of environmentally friendly, clean, and renewable energy sources and their further increase in utilization have become a consensus and development strategy in many countries [1]. Solar energy is an ideal alternative to traditional energy sources because of its cleanliness, accessibility, and abundance [2,3]. How to obtain and utilize solar energy more efficiently has been a hot research topic for scholars in recent years [4,5].

At present, solar energy utilization methods mainly include photovoltaic conversion and solar thermal conversion. Solar photovoltaic/thermal (PV/T) utilization systems that combine the two conversions can increase the efficiency of integrated solar energy utilization [6,7]. This system usually uses a cooling medium (e.g., water, air, etc.) to flow over the surface or backside of the cell to lower the cell temperature and remove and utilize the excess heat that affects power generation efficiency [8]. Due to the mutual thermal coupling between PV modules and the cooling medium in the system, the power generation efficiency of PV cells is directly affected by the temperature of the cooling medium. To ensure the conversion efficiency of photovoltaic devices, the cooling medium temperature is not high, and the effective utilization rate of heat is low. The proposed spectral beam splitting technology can avoid the problems of thermal coupling of PV and solar thermal utilization in PV/T systems [9,10]. Spectral beam splitting technology aims to use different wavelengths of light from the sun separately: Allocate the energy in solar radiation corresponding to the response band of photovoltaic cells to solar cells for photoelectric conversion; allocate solar radiation with higher thermal effect to solar thermal receivers for photothermal conversion [9,11]. Solar energy spectral beam splitting

technology, while avoiding overheating caused by solar radiation energy projected onto PV cells in the PV response band, can independently convert solar radiation energy in these bands for photothermal conversion, thus obtaining a higher overall efficiency [12,13].

Nanofluid-based spectral beam-splitting techniques have become popular for research in recent years. When the particle size of the material reaches the nanometer level, it has a small size effect, quantum size effect, surface effect and macroscopic quantum tunneling effect, and its behavior is closer to that of liquid molecules. Meanwhile, certain metal oxide nanomaterials strongly absorb solar radiation in the corresponding wavelength range due to their specific photonic forbidden band values, allowing enhanced heat and mass transfer and spectral beam splitting utilization.

The effect of nanofluids (such as CuO [14], Al₂O₃ [15,16], TiO₂ [17], and ZnO [18,19]) on PV/T systems has been investigated in numerical and experimental studies.

Wu [20] investigated the impact of air-cooling channel location on heat transfer characteristics and PV panel efficiency. Abdollahi [21] experimentally investigated the effect of natural nanofluid circulation and PCM on PV panels. In this work, the heat will be transferred from the nanofluid used to cool the PV panel to the phase-change material tank. They found that the power generation using natural nanofluid circulation and PCM at solar intensities (410, 530 and 690 W/m²) was increased by 44.74%, 46.63% and 48.23%, respectively, compared to the conventional case.

Tarun Mitta [22] presented a nanofluid-based dual-channel PV/T system and simulated it numerically. The results show a slight decrease in the electrical efficiency part, but the thermal efficiency is higher than that of the single-channel split-frequency PV/T system, making the dual-channel system a better choice.

Samir [23] proposed a new cascading nanofluid-based PV/T configuration with separate channels. The performance of the PV/T with separate channels (D-1) was compared with the double-pass channel (D-2). The simulation results show that the separate channel system (D-1) outperformed the double-pass design (D-2) by ~8.6%.

After reviewing references [20–23], it is not difficult to find that most studies focused on optical filtration effects and investigated the overall efficiency, including electrical and thermal efficiencies. There are few studies on fluid flow and temperature distribution in channels in PV/T systems. The uniform temperature distribution in the channel affects the overall efficiency of the PV/T system to some extent. Optimizing the arrangement of the interlayer inlet of frequency division components and uniform temperature distribution in the interlayer is beneficial to improve the photothermal conversion efficiency of the PV/T system.

In this paper, a PV/T integrated utilization module is designed and processed based on the already produced ZnO nanofluid. A simulation study of the flow characteristics of the ZnO nanofluid in the spectral beam splitting module was done, and an ideal flow method was identified to ensure a uniform temperature distribution on the surface of the PV cell while obtaining considerable heat and improving the integrated utilization efficiency.

2. Preparation and Optical Properties Characterization of ZnO Nanofluids

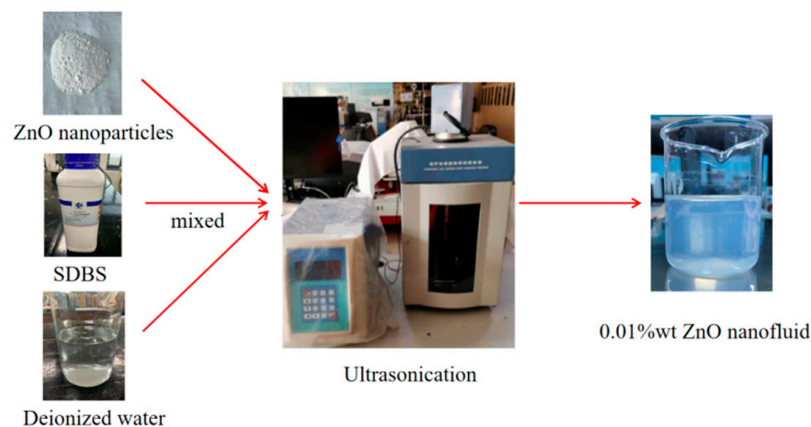
2.1. Preparation of Nanofluids

There are two main methods for preparing nanofluids: one-step and two-step methods. The one-step method disperses the particles into the base fluid while the particles are being prepared. The two-step method includes the selection of nanoparticles, the selection of dispersant and the ultrasonic dispersion of the suspension. The advantages of preparing nanofluids by the two-step method are that it is relatively simple and easy to control the concentration of the suspension, which helps further research work.

The ZnO nanofluid with a mass fraction of 0.01% was prepared by the two-step method. The material reagent parameters used for the preparation are shown in Table 1. Figure 1 shows the preparation process of ZnO nanofluids.

Table 1. Materials and reagents.

Name	Parameter
Nano ZnO powder	Purity: 99.9%
SDBS (Sodium dodecylbenzene sulfonate)	Average particle size: 30 nm
	Purity: >90%

**Figure 1.** Process of ZnO nanofluids preparation.

2.2. Optical Properties of Nanofluids

The band gap of ZnO is 3.2 eV, corresponding to an absorption wavelength of 388 nm. Due to the quantum size effect, the band gap increases to 4.5 eV for a ZnO nanoparticle size of 10 nm. By scattering and absorption of UV light, ZnO nanomaterials have excellent UV shielding effects.

To meet the characteristics of ZnO nanofluid as a spectral beam-splitting heat collector with a certain absorbance while ensuring a high transmittance, the final ZnO nanofluid of 0.01 wt% was made through experiments. The fabricated nanofluid was tested for optical properties by UV-3600 UV-Vis NIR spectrophotometer, mainly for transmittance and absorbance measurements. The test results are shown in Figures 2 and 3.

As shown in Figure 2, compared with DI (Deionized water), the transmittance of the resulting ZnO nanofluid varies consistently with a wavelength in the visible light range of 400–800 nm, and the degree of attenuation is within 10%. This indicates that the ZnO nanoparticles do not have strong absorption of solar radiation in the visible wavelength range, which can ensure that the irradiation in the effective wavelength range that is beneficial to the power generation of PV panels is irradiated to the surface of PV panels through the fluid. The transmission of the visible ZnO nanofluid decreases steeply around 380 nm, indicating that it has very strong absorption of UV light near this wavelength.

Compared with DI (deionized water), the absorbance of the resulting ZnO nanofluid in the visible light range of 400–800 nm showed the same trend with wavelength, and the degree of attenuation was within 0.1, as illustrated in Figure 3. This means that the absorption of solar radiation in the visible wavelength range of ZnO nanoparticles is not much different from that of DI, which can ensure that the irradiation in the effective wavelength range beneficial to the power generation of PV panels can be irradiated to the surface of PV panels through the fluid. The visible ZnO nanofluid has an obvious absorption peak of around 380 nm. Still, it maintains an absorption value of about 1.25 between 230 and 380 nm, indicating a strong absorption effect on UV light in this wavelength band.

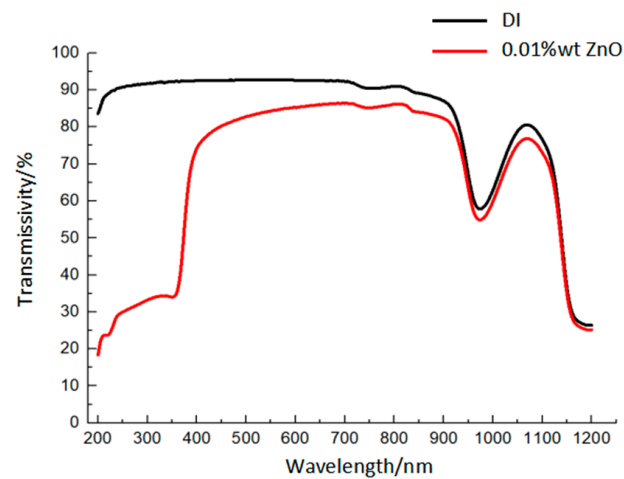


Figure 2. Curves of 0.01 wt% ZnO nanofluid transmittance as a function of wavelength.

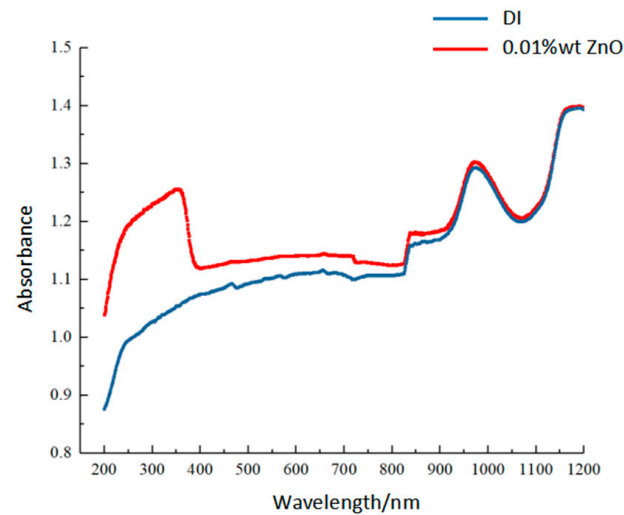


Figure 3. The curve of absorbance of 0.01 wt% ZnO nanofluid as a function of wavelength.

3. Spectral Beam Splitting Module and Physical Model Settings

3.1. Spectral Beam Splitting Module and Parameters

The physical PV/T spectral beam splitting module is shown in Figure 4, and the dimensions are shown in Table 2. To ensure the nanofluid's effective absorption of solar radiation and to consider the physical strength and economy of the module, the surface is encapsulated with an ultra-white glass of 5 mm thickness.

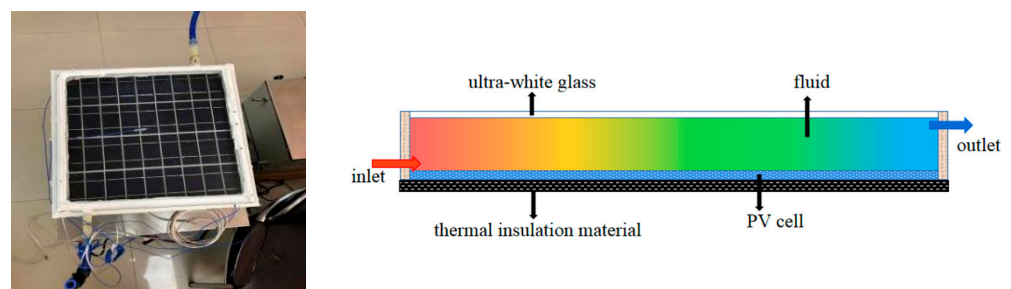


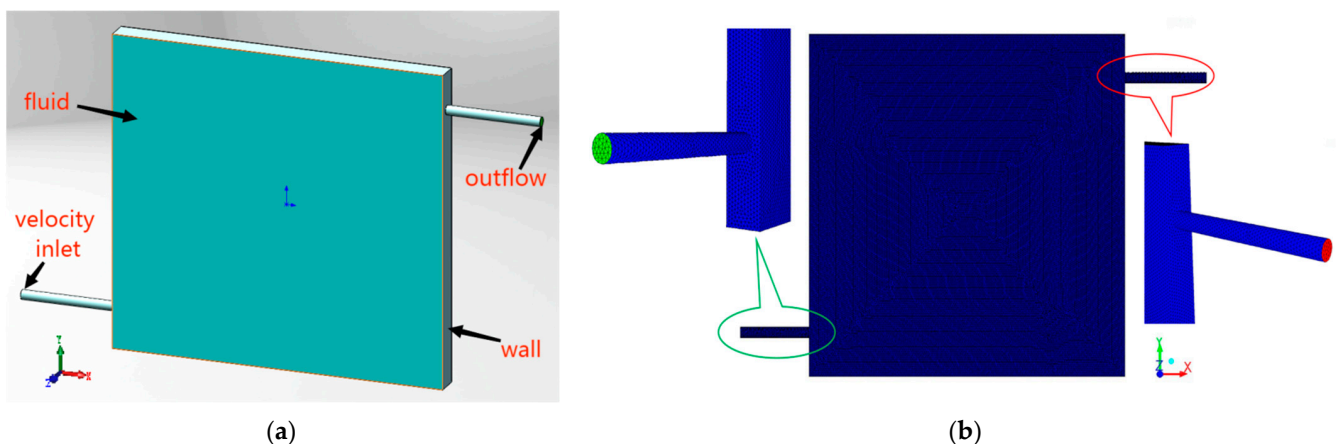
Figure 4. Schematic diagram and picture of PV/T spectral beam splitting module.

Table 2. Geometric Size of spectral beam splitting module.

Geometric Parameters/mm	Values
Length/L	350
Width/W	330
Height/H	25
Interlayer thickness/M	20
Inlet and outlet pipe diameter/D	10
Pipe thickness/d	1

3.2. Physical Model and Boundary Condition Settings

To simulate the flow state and heat transfer of a nanofluid in the interlayer of the splitting module more accurately and conveniently, this experiment simplifies the actual module into a three-dimensional rectangular interlayer with an inlet and outlet. The geometric dimensions are kept the same as the actual ones. The computational domain diagram is shown in Figure 5a. The six boundary surfaces are set adiabatically, excluding other variables, and the influence of the inlet end on the flow state and heat transfer uniformity of the fluid inside the interlayer is studied purely. Assume that the angle between the light-receiving surface and gravity direction is 130° , and the nanofluid inside the interlayer is simplified to a liquid with the same thermal conductivity and viscosity as the actual fluid. The inlet flow rate is set to 0.533 m/s, the inlet temperature is 313 K, and the initial temperature is 298 K, which is imported into ANSYS for transient simulation. The walls are set to be insulated and have no-slip boundary conditions. The simulation variables are the length of the inlet pipe inserted into the cavity, the position, and the distribution of the water divider.

**Figure 5.** Computational domain and mesh for the PVT system. (a) Computational domain; (b) mesh.

The nanofluid is considered to be incompressible Newtonian fluid. The 3-D model of the system was numerically simulated by ANSYS Fluent. The grid is shown in Figure 5b. The control conservation equation is discretized by the finite volume method. The pressure basis scheme is used to solve the conservation equations. The SIMPLE method considers the coupling of pressure and velocity, and the convection terms are discretized by second-order upwind [24,25]. The inlet mass flow rate is 0.042 kg/s, and the Reynolds number is 5273. Turbulence model using k- ϵ standard model.

3.3. Mathematical Model

Mass equation

$$\frac{\partial \rho}{\partial t} + \frac{\partial(\rho u)}{\partial x} + \frac{\partial(\rho v)}{\partial y} + \frac{\partial(\rho w)}{\partial z} = 0 \quad (1)$$

Momentum equation

$$\frac{\partial(\rho u)}{\partial t} + \frac{\partial(\rho u u)}{\partial x} = \frac{\partial}{\partial x} \left(\mu \frac{\partial u}{\partial x} \right) - \frac{\partial P}{\partial x} \quad (2)$$

$$\frac{\partial(\rho v)}{\partial t} + \frac{\partial(\rho v v)}{\partial y} = \frac{\partial}{\partial y} \left(\mu \frac{\partial v}{\partial y} \right) - \frac{\partial P}{\partial y} \quad (3)$$

$$\frac{\partial(\rho w)}{\partial t} + \frac{\partial(\rho w w)}{\partial z} = \frac{\partial}{\partial z} \left(\mu \frac{\partial w}{\partial z} \right) - \frac{\partial P}{\partial z} \quad (4)$$

Energy equation

$$\rho C_p \left(u \frac{\partial T}{\partial x} + v \frac{\partial T}{\partial y} + w \frac{\partial T}{\partial z} \right) = k \left(\frac{\partial^2 T}{\partial x^2} + \frac{\partial^2 T}{\partial y^2} + \frac{\partial^2 T}{\partial z^2} \right) \quad (5)$$

where ρ represents fluid density, u , v , and w are velocity components in x , y and z , respectively, P is pressure, μ is dynamic viscosity, C_p is specific heat capacity, and k is thermal conductivity.

3.4. Grid and Time Independence Study and Model Validation

The grid independence study of the module is conducted by generating different grid numbers of 500, 1000, 2000, 2600, 3700, 4300, and 5000 thousand. Grids are three-dimensional and unstructured. A detailed grid diagram is shown in Figure 5b. The outlet temperature for different mesh numbers is presented in Figure 6a. The reason for choosing 2.6 million is that the PV/T outflow temperature is almost the same when the number of grids is greater than 2.6 million. The minimum grid size of 0.5 mm. The suitable time step is also determined according to the outlet temperature difference of the system for seven-time steps of 0.1 s, 0.2 s, 0.5 s, 1 s, 1.5 s, 2 s and 2.5 s. Figure 6b illustrates the outlet temperature difference in the simulations with various time step sizes. Therefore, the step size of 0.5 s is chosen.

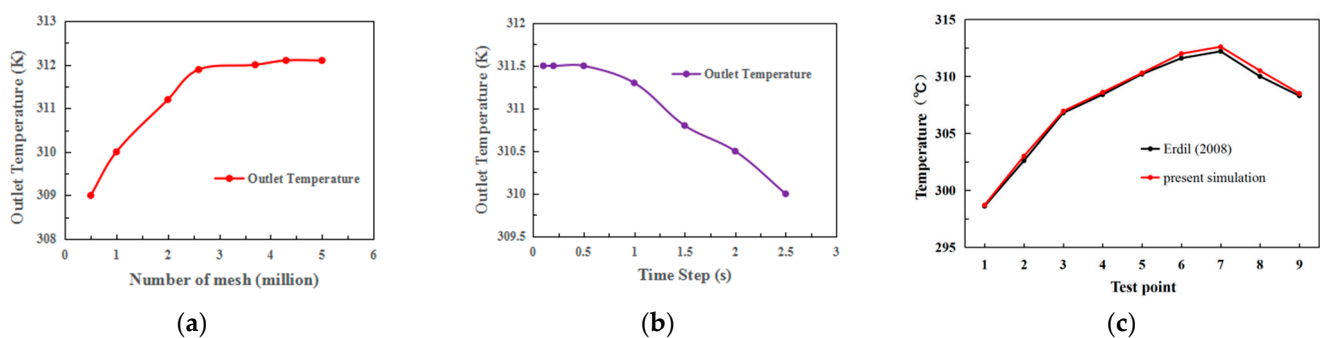


Figure 6. Grid and time independence study and mathematical model validation. (a) Grid independence study; (b) Time independence study; (c) mathematical model validation [26].

To prove the accuracy of this mathematical model, the related parameters are set equally with that in the reference [26]. For example, the mass flow rate is 18 L/h, the inlet water temperature is 297 K, the collector slope is 45, and the interlayer thickness is 5 mm. The calculated outlet temperature matched the tested results in Ref. [26] (Figure 6c).

4. Analysis of Simulation Results

For the convenience of description, the following simulation results are labeled as case I, case II, case III, case IV, case V and case VI, according to the different arrangements at the inlet end. The details of the arrangement are as follows.

Case I: The inlet end is set in the lower left of the interlayer, and the outlet end is upper right, and the schematic diagram of the length of the inlet end is shown in Figure 5a.

Case II: The inlet end is set at the lower left of the interlayer, the outlet end is upper right, and the inlet pipe is inserted into the inner part of the interlayer, with nine water-dividing holes of 4 mm in diameter. The hole spacing is 30 mm, and the end of the pipe is sealed. The schematic diagram is shown in Figure 7a.

Case III: The inlet end is set at the lower left of the interlayer, the outlet end is at the upper right, the inlet pipe is inserted into the inner part of the interlayer, and the lower part is opened with nine 4 mm diameter water distribution holes with a hole spacing of 30 mm, and the end of the pipe is sealed. The schematic diagram is shown in Figure 7b.

Case IV: The inlet end is set at the bottom of the left side of the interlayer, with the outlet pipe at an angle of 90° , the outlet end is on the right, and the inlet pipe is inserted into the interior of the interlayer, and nine water distribution holes with a diameter of 4 mm are opened to the side of the outlet end, with a hole spacing of 30 mm, and the end of the pipe is sealed. The schematic diagram is shown in Figure 7c.

Case V: The inlet end is set at the lower left of the interlayer, the outlet end is at the upper right, and the inlet pipe is inserted into the inner part of the interlayer, with four water distribution holes of 4 mm diameter at the lower part and five water distribution holes of 4 mm diameter at the upper part, with a hole spacing of 30 mm, and the end of the pipe is not sealed. The schematic diagram is shown in Figure 7d.

Case VI: The inlet end is set at the lower left side of the interlayer, the outlet end is at the upper right side, and the inlet pipe is inserted into the inner part of the interlayer, with four water distribution holes of 4 mm diameter at the lower part and five water distribution holes of 4 mm diameter at the upper part, with a hole spacing of 30 mm, and the end of the pipe is sealed. The schematic diagram is shown in Figure 7e.

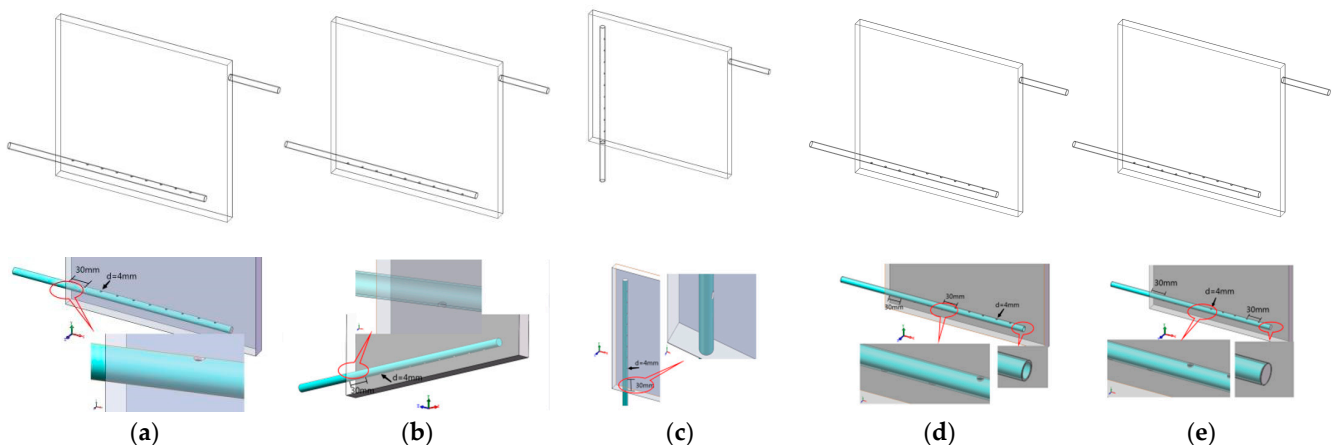


Figure 7. Diagram of the different arrangements at the inlet end of the interlayer (a) case II; (b) case III; (c) case IV; (d) case V; (e) case VI.

4.1. Analysis of Flow Characteristics under Different Arrangements at the Inlet End

For the sake of description, the central cross-section parallel to the supposed light-receiving surface is called the transverse cross-section, while the central cross-section perpendicular to the supposed light-receiving surface is referred to as the longitudinal cross-section.

Figure 8a shows the velocity distribution of the cross-section under case II. As shown in the figure, the velocity distribution in this plane does not change from 50 s to 250 s under the two-dimensional plane of flow, and it can be seen that the flow velocity is greater near the diversion orifice near the outlet because the local pressure is smaller there compared to that near the inlet section. The outlet end of the orifice suddenly contracted, so the fluid flow velocity increased. The velocity distribution under case III is similar to that of case II (Figure 8b), but the flow velocity near the diversion holes is more uniform than that of case II. As for the case IV in Figure 8c, even though there is gravitational influence, the

direction of flow out of the diversion holes is still biased toward the outlet end, and the flow is stronger on the upper side of the diversion holes than on the lower side.

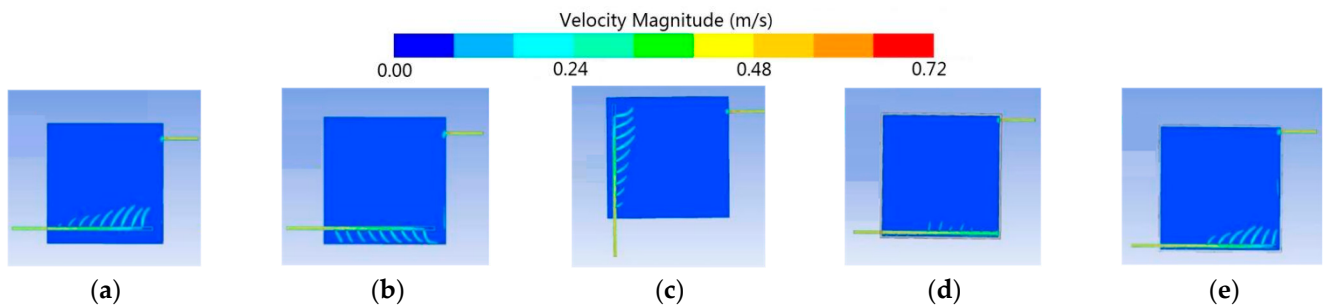


Figure 8. Velocity distribution of the cross-section (a) case II (b) case III (c) case IV (d) case V (e) case VI.

As seen in Figure 8d, unlike case III, the splitting pressure of the splitting holes is smaller because the end of the inlet pipe is not sealed. The velocity distribution is not obvious, and the first and last few diversion holes are smaller than the middle water flow. Due to the sealing of the end of the inlet pipe under the case VI (Figure 8e), the diversion hole partial pressure increases, and the end diversion hole water flow rate increases compared to case V.

A more apparent counterclockwise backflow is formed in the interlayer space at the upper end of the inlet pipe under case II (Figure 9a). Analysis of the reason, the right outlet suddenly contracted, part of the fluid flow velocity increased to discharge the interlayer, and the other part went back along the inner wall of the interlayer, forming a gyration. The gyration center fluid flow rate is slower. Inlet pipe with the pipe length flow rate slowed down, but the back end of the water splitting hole flow rate is greater than the front, mainly because of the difference in pressure near the water splitting hole.

Figure 9b shows the cross-sectional velocity vector diagram in case III. The circulation in the central space of the interlayer is not apparent, and the fluid flows out more along the lower wall through the right wall. The velocity distribution is denser along the right wall. The lower opening of the diversion hole makes the fluid flow out and back in other directions after flowing against the lower side wall.

As shown in Figure 9c, the fluid forms a clockwise return flow in the center space of the mezzanine, which is more similar to the case II. A small vortex with counterclockwise flow is formed in the upper left corner at the end of the inlet pipe due to the blockage of the wall.

As shown in Figure 9d, the vortex in the upper left corner gradually decreases with time. The lower right corner forms a delta of velocity vector distribution with more obvious demarcation because the pressure on both sides is different due to the unsealed end, resulting in different flow field distributions, and a region of slower flow velocity is formed between the diagonals.

Compared with case V, the velocity vector in case VI (Figure 9e) almost does not change with time. The same gyration is formed in the center space of the interlayer, and the velocity distribution is denser along the right side of the wall. The direction of the water outlet from the diversion hole is biased towards the direction of the outlet end. The reason is more similar to case II and will not be repeated.

The above comparison shows that the fluid velocity distribution in the interlayer tends to stabilize after a short time of formation. The inlet end arrangement has a more obvious effect on the flow field distribution, and various arrangements have produced different sizes of gyration and slower flow areas.

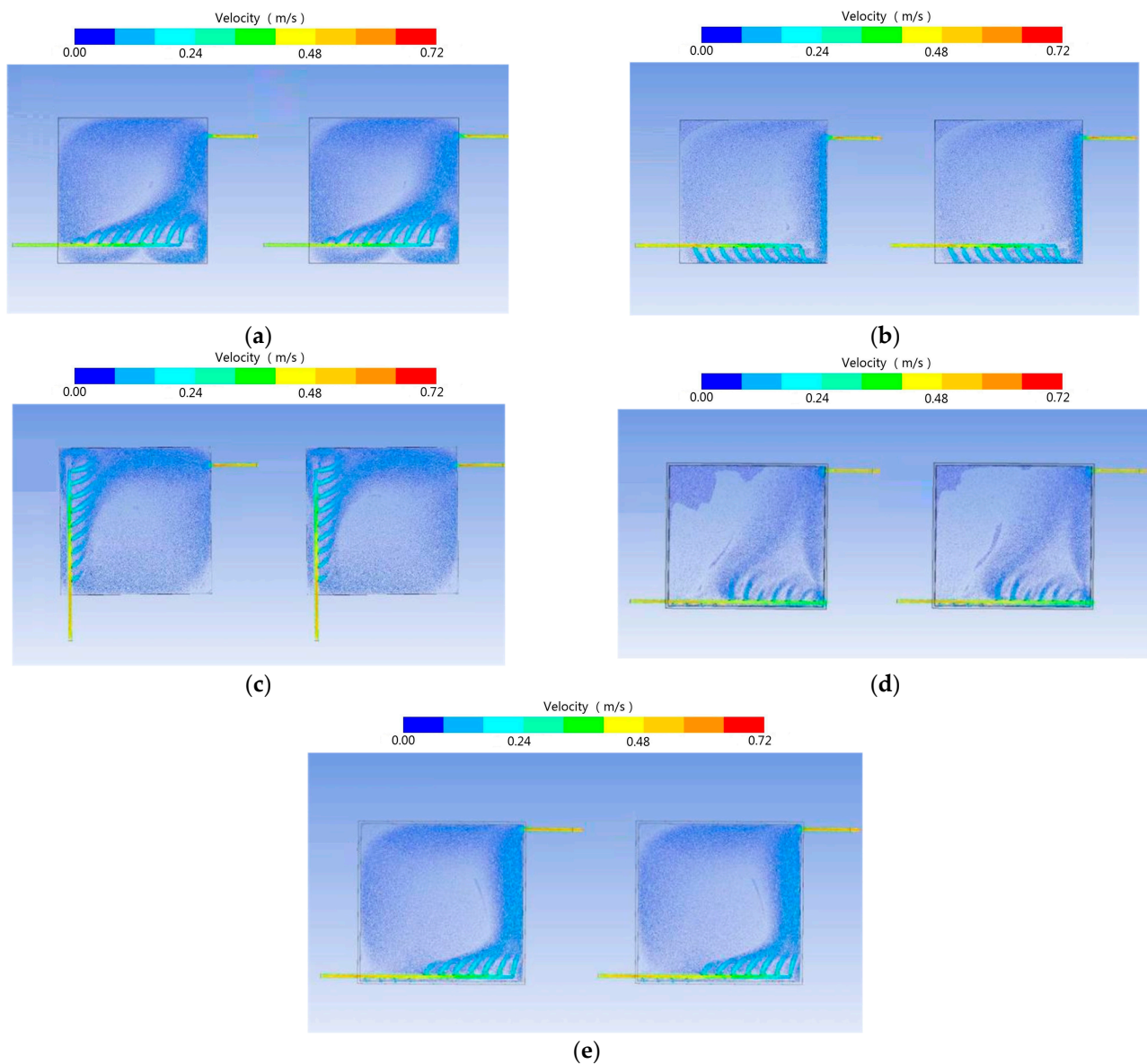


Figure 9. Velocity vector diagram of the cross-section at the same time node (a) case II (b) case III (c) case IV (d) case V (e) case VI.

4.2. Convective Heat Transfer Characteristics Analysis

For solar thermal utilization, the uniformity of the temperature field is crucial. On the one hand, a better temperature distribution can improve the thermal efficiency of the collector system. On the other hand, it can also avoid damage to the modules due to thermal stresses caused by temperature differences. For fractional frequency modules, the uniformity of the temperature distribution also affects the circulation performance of the fractional nanofluid and the photovoltaic conversion efficiency of the PV panel.

The temperature distribution of the cross-section at different time nodes under case I is shown in Figure 10. The lower side and right-side walls reach the highest temperature in the interlayer first. Because of the rotation in the center of the interlayer, the fluid flow in the center is slow, compared to the surrounding convective heat transfer is very weak, so there is a “leafy” low-temperature zone, and the temperature distribution is not uniform. The upper left corner is also a small area of low-temperature zone formed due to the slow flow and weak heat transfer. After 400 s, the maximum temperature difference reaches about 9 °C.

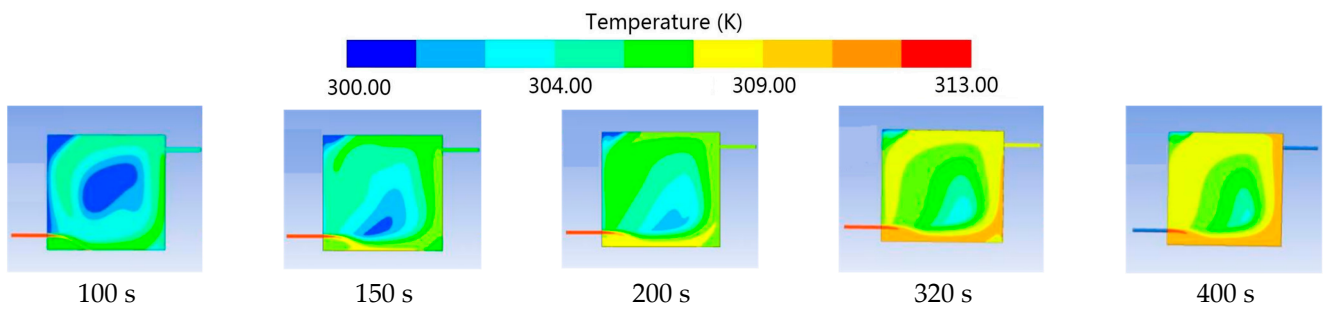


Figure 10. Temperature distribution of cross-section at different time nodes under Case I.

As illustrated in Figure 11, the velocity field is more uniformly distributed than that of case I. Hence, the “leafy” area formed in the center of the interlayer is smaller than that of case I. The maximum internal temperature difference is only 2 °C after 450 s of flow. However, the temperature is more likely to converge over time because of the stronger convective heat transfer around it. As shown in Figure 12, the distribution is more uniform in the longitudinal depth and close to the symmetric distribution.

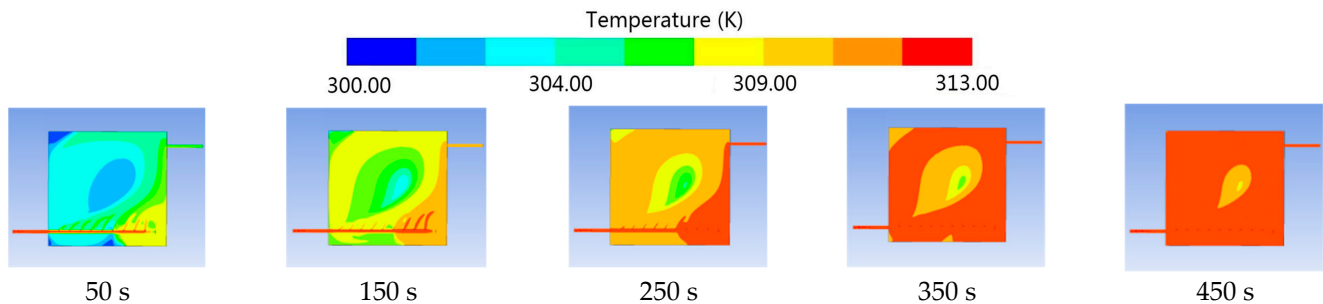


Figure 11. Temperature distribution of cross-section at different time nodes under case II.

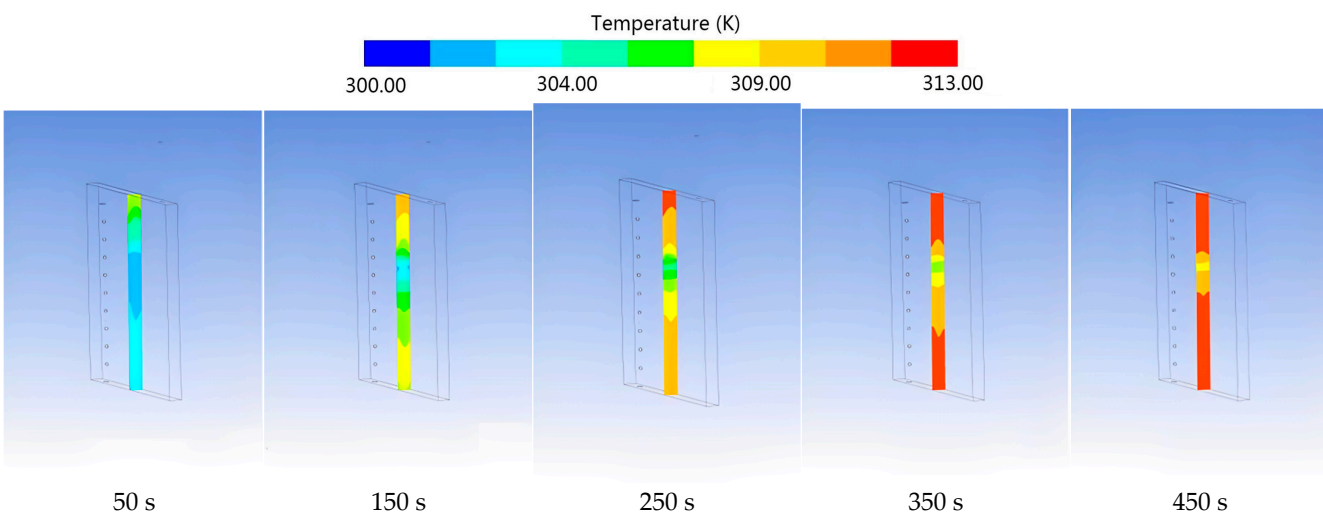


Figure 12. Temperature distribution of longitudinal section at different time nodes under case II.

Compared with the arrangement of case II, the formation of gyration in case III at the same time node is relatively late, and the area of the “leafy” low-temperature zone formed in the center is smaller with time, but there is an obvious heat transfer hysteresis zone in the upper left corner (as exhibited in Figure 13). Referring to Figure 14, the temperature distribution in the longitudinal section is more uniform than that in case II. However, the temperature in the lower part of the longitudinal section is lower in the early stage of convection heat transfer.

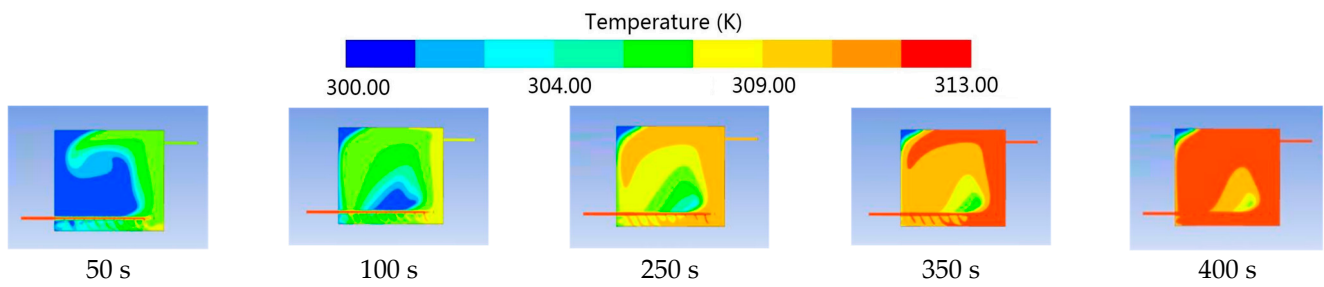


Figure 13. Temperature distribution of cross-section at different time nodes under case III.

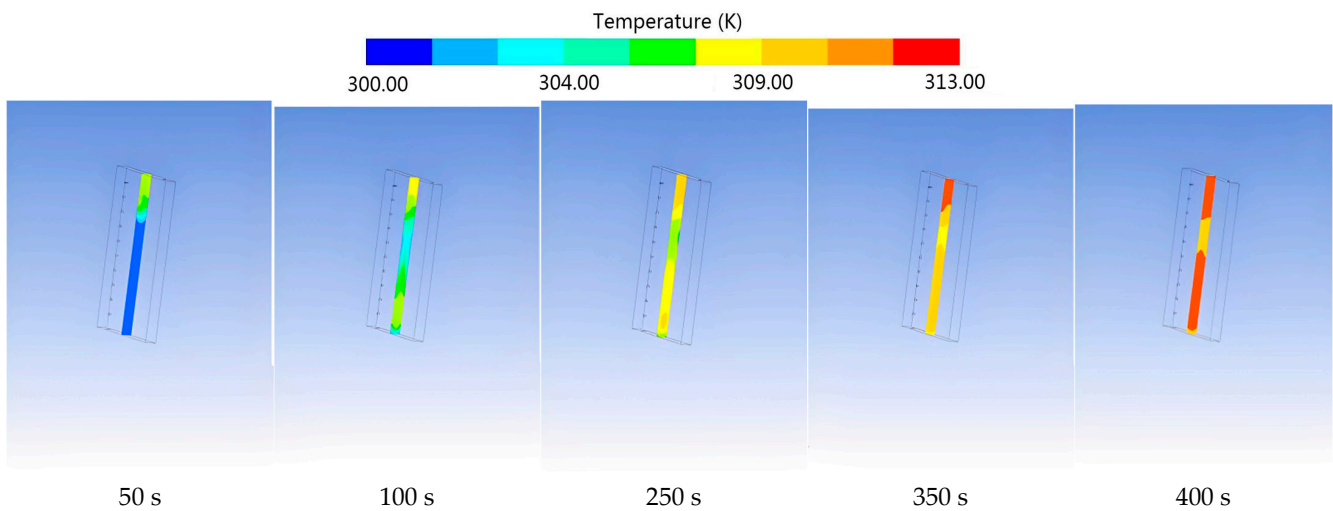


Figure 14. Temperature distribution of longitudinal section at different time nodes under case III.

The temperature distribution at 50 s in Figure 15 is similar to case III, but the temperature gradient is obviously smaller. The area of the lowest temperature point in the center of the “leafy” low-temperature zone formed in the center is smaller. In contrast, the four corners do not form a heat transfer hysteresis zone, and the temperature distribution is more uniform. Combined with Figure 16, it is similar to case III, and the distribution is more ideal.

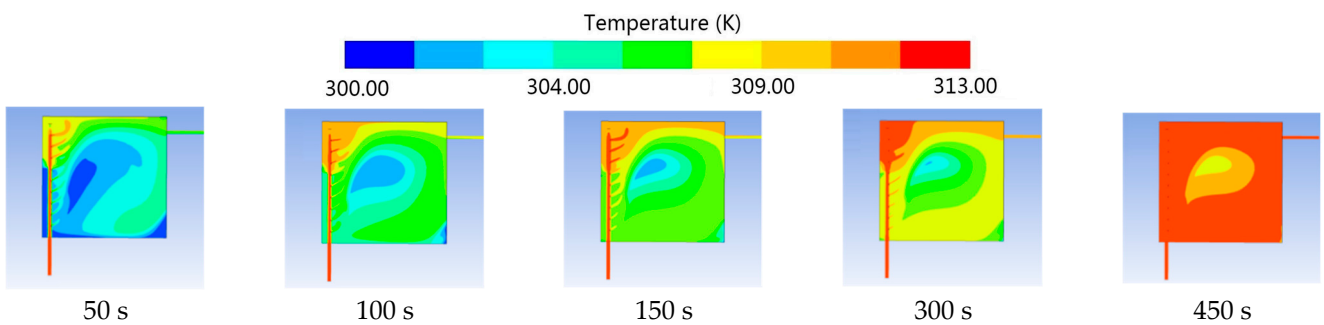


Figure 15. Temperature distribution of cross-section at different time nodes under case IV.

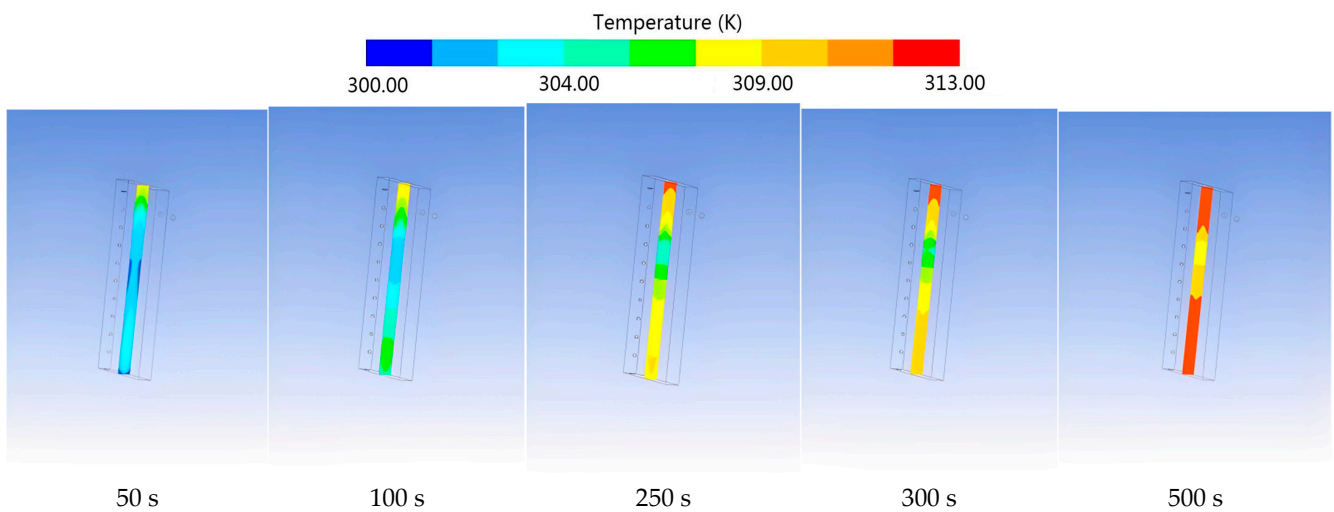


Figure 16. Temperature distribution of longitudinal section at different time nodes under case IV.

Since the end of case V inlet pipe is not sealed, convective heat exchange from the beginning of the flow is mainly concentrated on the side of the end opening. In contrast, the relative side maintained the initial temperature after the flow proceeded to 400 s, indicating that convective heat exchange near this place is extremely weak (Figure 17). The temperature distribution in Figure 18 is stepped, with poor uniformity.

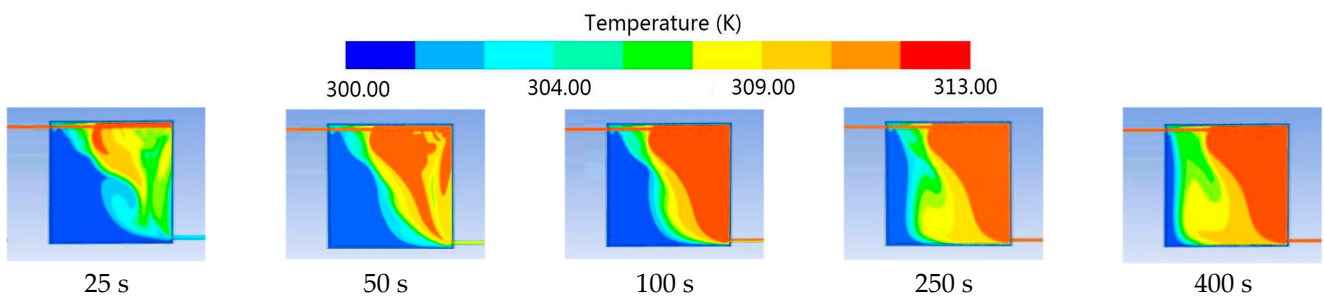


Figure 17. Temperature distribution of cross-section at different time nodes under case V.

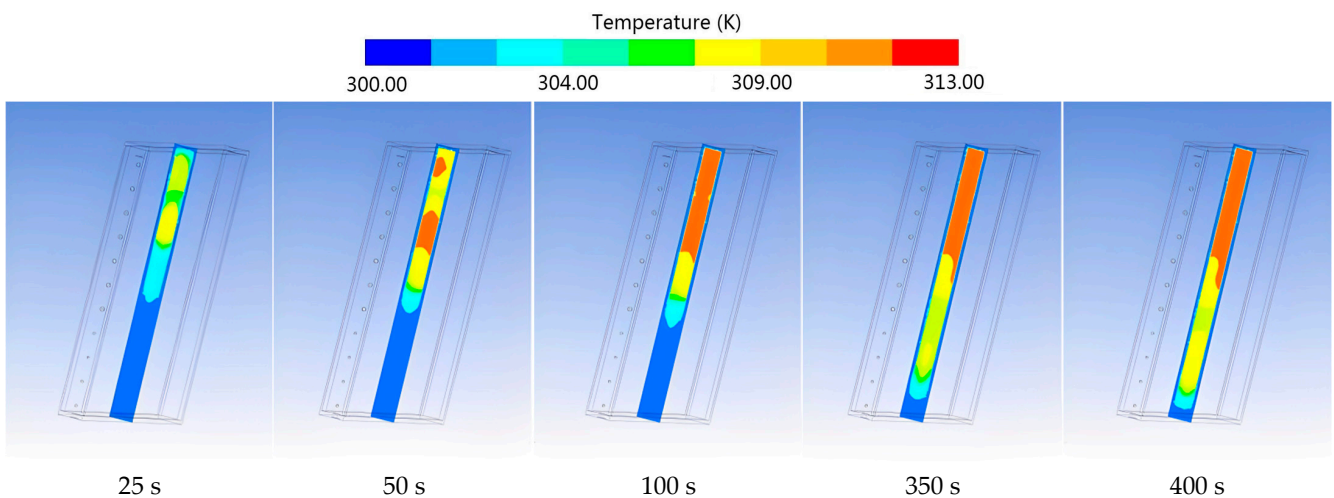


Figure 18. Temperature distribution of longitudinal section at different time nodes under case V.

As shown in Figure 19, compared with case V, an obvious “leafy” low-temperature zone is formed. Compared with the previous arrangements, case VI has a wider range of

lower temperatures in the center, and the adjacent temperature difference is not large, but the heat transfer efficiency is lower, and the overall temperature at the same time node is lower than the other arrangements. Similar conclusions can be drawn by referring to Figure 20.

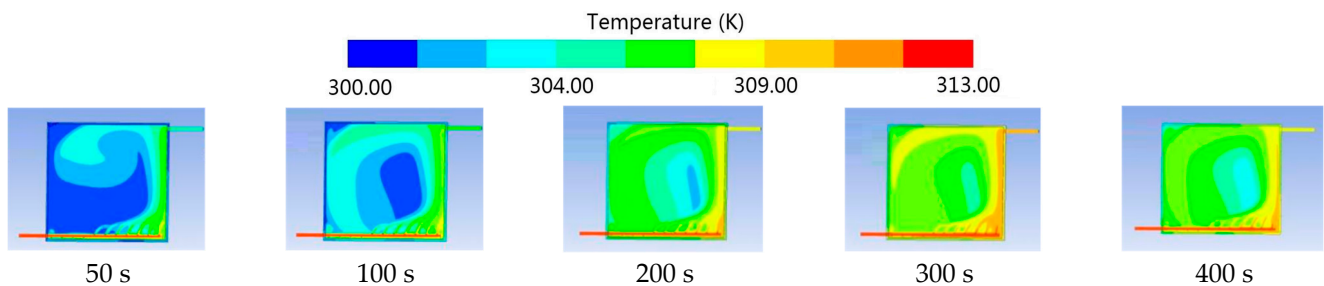


Figure 19. Temperature distribution of cross-section at different time nodes under case VI.

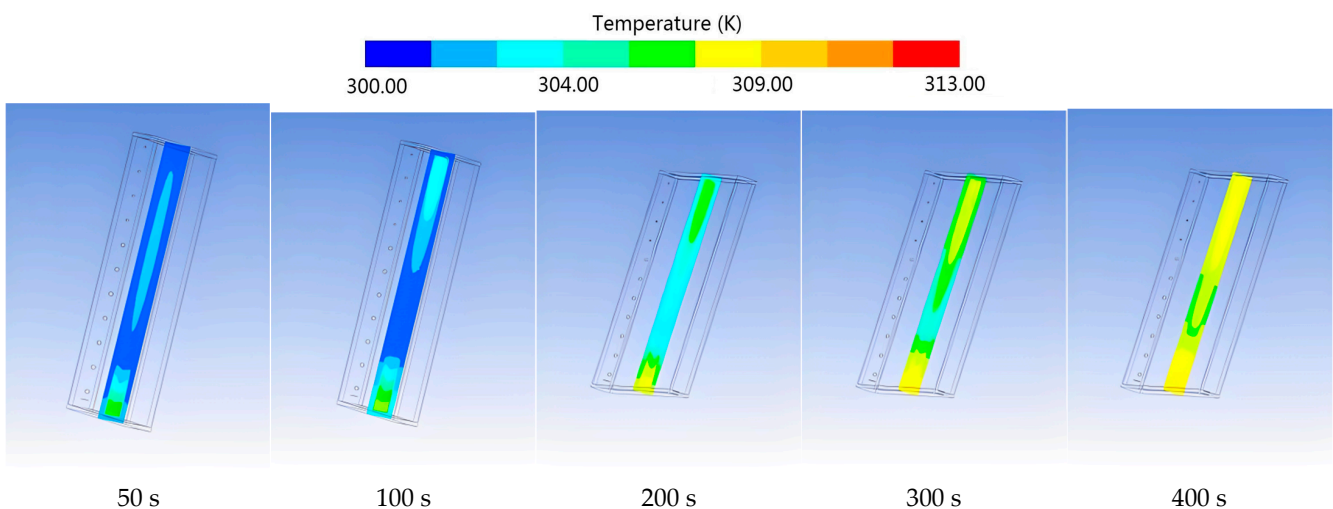


Figure 20. Temperature distribution of longitudinal section at different time nodes under case VI.

5. Conclusions

Increasing energy utilization and comprehensive efficiency of conventional PV/T integrated utilization systems using nanofluid have been hot research topics in recent years. The use of frequency-divided nanofluid to improve the efficiency of PV/T integrated utilization system has high requirements on the flow characteristics of nanofluid and the arrangement of frequency-divided components. In this paper, we simulated the arrangement of the nanofluid inlet of the split-frequency module based on the existing experimental components to obtain a more optimal arrangement. The following conclusions are obtained from the simulations.

1. The shorter the inlet end is, the more uneven the velocity distribution of the interlayer fluid is, which leads to the smaller intensity of convective heat transfer within the interlayer and the uneven distribution of the temperature field.
2. Case II and case III are more ideal, of which case II is the most ideal. Analysis of the reasons, case II velocity field distribution, is more uniform. It indicates that the fluid flow state and the flow velocity distribution play a decisive role in the uniformity of temperature distribution.
3. The cross-sectional area of the central “leafy” low-temperature region resulting from different arrangements is not the same, indicating that the central cross-section/s temperature field distribution is not symmetric. The temperature field distribution at the cross-section is similar, but the temperature field is different in the direction of interlayer thickness.

Author Contributions: Conceptualization, R.T.; Software, X.H.; Data curation, L.L.; Writing—original draft, X.H.; Writing—review & editing, L.L.; Supervision, R.T.; Funding acquisition, R.T. All authors have read and agreed to the published version of the manuscript.

Funding: This work was supported by the Inner Mongolia Science and Technology Major Project (NO. 2019ZD014).

Data Availability Statement: The data presented in this study are available on request from the corresponding author.

Conflicts of Interest: The authors declare no conflict of interest.

References

1. Kuşkaya, S.; Bilgili, F.; Muğaloğlu, E.; Khan, K.; Hoque, M.E.; Toguç, N. The role of solar energy usage in environmental sustainability: Fresh evidence through time-frequency analyses. *Renew. Energy* **2023**, *206*, 858–871. [\[CrossRef\]](#)
2. He, Q.; Wang, S.; Tong, M.; Liu, Y. Experimental study on thermophysical properties of nanofluids as phase-change material (PCM) in low temperature cool storage. *Energy Convers. Manag.* **2012**, *64*, 199–205. [\[CrossRef\]](#)
3. Chen, N.; Ma, H.; Li, Y.; Cheng, J.; Zhang, C.; Wu, D.; Zhu, H. Complementary optical absorption and enhanced solar thermal conversion of CuO-ATO nanofluids. *Sol. Energy Mater. Sol. Cells* **2017**, *162*, 83–92. [\[CrossRef\]](#)
4. Sajid, M.U.; Bicer, Y. Nanofluids as solar spectrum splitters: A critical review. *Sol. Energy* **2020**, *207*, 974–1001. [\[CrossRef\]](#)
5. Otanicar, T.P.; Phelan, P.E.; Prasher, R.S.; Rosengarten, G.; Taylor, R.A. Nanofluid-based direct absorption solar collector. *J. Renew. Sustain. Energy* **2010**, *2*, 33102. [\[CrossRef\]](#)
6. Zondag, H. Flat-plate PV-Thermal collectors and systems: A review. *Renew. Sustain. Energy Rev.* **2008**, *12*, 891–959. [\[CrossRef\]](#)
7. Kumar, R.; Rosen, M.A. A critical review of photovoltaic–thermal solar collectors for air heating. *Appl. Energy* **2011**, *88*, 3603–3614. [\[CrossRef\]](#)
8. Huaxu, L.; Fuqiang, W.; Dong, Z.; Ziming, C.; Chuanxin, Z.; Bo, L.; Huijin, X. Experimental investigation of cost-effective ZnO nanofluid based spectral splitting CPV/T system. *Energy* **2020**, *194*, 116913. [\[CrossRef\]](#)
9. Blocker, W. High-efficiency solar energy conversion through flux concentration and spectrum splitting. *Proc. IEEE* **1978**, *66*, 104–105. [\[CrossRef\]](#)
10. Jiang, S.; Hu, P.; Mo, S.; Chen, Z. Optical modeling for a two-stage parabolic trough concentrating photovoltaic/thermal system using spectral beam splitting technology. *Sol. Energy Mater. Sol. Cells* **2010**, *94*, 1686–1696. [\[CrossRef\]](#)
11. Imenes, A.; Mills, D. Spectral beam splitting technology for increased conversion efficiency in solar concentrating systems: A review. *Sol. Energy Mater. Sol. Cells* **2004**, *84*, 19–69. [\[CrossRef\]](#)
12. Hu, P.; Zhang, Q.; Liu, Y.; Sheng, C.; Cheng, X.; Chen, Z. Optical analysis of a hybrid solar concentrating Photovoltaic/Thermal (CPV/T) system with beam splitting technique. *Sci. China Technol. Sci.* **2013**, *56*, 1387–1394. [\[CrossRef\]](#)
13. Liu, M.; Du, M.; Long, G.; Wang, H.; Qin, W.; Zhang, D.; Ye, S.; Liu, S.; Shi, J.; Liang, Z.; et al. Iron/Quinone-based all-in-one solar rechargeable flow cell for highly efficient solar energy conversion and storage. *Nano Energy* **2020**, *76*, 104907. [\[CrossRef\]](#)
14. Hajabdollahi, Z.O.; Mirzaei, M.; Kim, K.C. Effects of a mixture of CuO and Al₂O₃ nanoparticles on the thermal efficiency of a flat plate solar collector at different mass flow rates. *Heat Transf. Res.* **2019**, *50*, 945–965. [\[CrossRef\]](#)
15. Sardarabadi, M.; Passandideh-Fard, M. Experimental and numerical study of metal-oxides/water nanofluids as coolant in photovoltaic thermal systems (PVT). *Sol. Energy Mater. Sol. Cells* **2016**, *157*, 533–542. [\[CrossRef\]](#)
16. Hissouf, M.; Feddaoui, M.; Najim, M.; Charef, A. Numerical study of a covered Photovoltaic-Thermal Collector (PVT) enhancement using nanofluids. *Sol. Energy* **2020**, *199*, 115–127. [\[CrossRef\]](#)
17. Farajzadeh, E.; Movahed, S.; Hosseini, R. Experimental and numerical investigations on the effect of Al₂O₃/TiO₂-H₂O nanofluids on thermal efficiency of the flat plate solar collector. *Renew. Energy* **2018**, *118*, 122–130. [\[CrossRef\]](#)
18. Wole-Osho, I.; Adun, H.; Adedeji, M.; Okonkwo, E.C.; Kavaz, D.; Dagbasi, M. Effect of hybrid nanofluids mixture ratio on the performance of a photovoltaic thermal collector. *Int. J. Energy Res.* **2020**, *44*, 9064–9081. [\[CrossRef\]](#)
19. Salari, A.; Kazemian, A.; Ma, T.; Hakkaki-Fard, A.; Peng, J. Nanofluid based photovoltaic thermal systems integrated with phase change materials: Numerical simulation and thermodynamic analysis. *Energy Convers. Manag.* **2020**, *205*, 112384. [\[CrossRef\]](#)
20. Wu, S.-Y.; Wang, T.; Xiao, L.; Shen, Z.-G. Effect of cooling channel position on heat transfer characteristics and thermoelectric performance of air-cooled PV/T system. *Sol. Energy* **2019**, *180*, 489–500. [\[CrossRef\]](#)
21. Abdollahi, N.; Rahimi, M. Potential of water natural circulation coupled with nano-enhanced PCM for PV module cooling. *Renew. Energy* **2019**, *147*, 302–309. [\[CrossRef\]](#)
22. Mittal, T.; Saroha, S.; Bhalla, V.; Khullar, V.; Tyagi, H.; Taylor, R.A.; Otanicar, T.P. Numerical Study of Solar Photovoltaic/Thermal (PV/T) Hybrid Collector Using Nanofluids. In Proceedings of the ASME 2013 4th International Conference on Micro/Nanoscale Heat and Mass Transfer, Hong Kong, China, 11–14 December 2013.
23. Hassani, S.; Taylor, R.A.; Mekhilef, S.; Saidur, R. A cascade nanofluid-based PV/T system with optimized optical and thermal properties. *Energy* **2016**, *12*, 963–975. [\[CrossRef\]](#)

24. Khatibi, M.; Nemati-Farouji, R.; Taheri, A.; Kazemian, A.; Ma, T.; Niazmand, H. Optimization and performance investigation of the solidification behavior of nano-enhanced phase change materials in triplex-tube and shell-and-tube energy storage units. *J. Energy Storage* **2021**, *33*, 102055. [[CrossRef](#)]
25. Kazemian, A.; Taheri, A.; Sardarabadi, A.; Ma, T.; Passandideh-Fard, M.; Peng, J. Energy, exergy and environmental analysis of glazed and unglazed PVT system integrated with phase change material: An experimental approach. *Sol. Energy* **2020**, *201*, 178–189. [[CrossRef](#)]
26. Erdil, E.; Ilkan, M.; Egelioglu, F. An experimental study on energy generation with a photovoltaic (PV)–solar thermal hybrid system. *Energy* **2008**, *33*, 1241–1245. [[CrossRef](#)]

Disclaimer/Publisher’s Note: The statements, opinions and data contained in all publications are solely those of the individual author(s) and contributor(s) and not of MDPI and/or the editor(s). MDPI and/or the editor(s) disclaim responsibility for any injury to people or property resulting from any ideas, methods, instructions or products referred to in the content.